UC Berkeley
UC Berkeley Previously Published Works

Title
Influence of iron doping on tetravalent nickel content in catalytic oxygen evolving films

Permalink
https://escholarship.org/uc/item/2p3410z1

Journal
Proceedings of the National Academy of Sciences of the United States of America, 114(7)

ISSN
0027-8424

Authors
Li, Nancy
Bediako, D Kwabena
Hadt, Ryan G
et al.

Publication Date
2017-02-14

DOI
10.1073/pnas.1620787114

Peer reviewed

eScholarship.org Powered by the California Digital Library
University of California

Influence of iron doping on tetravalent nickel content in catalytic oxygen evolving films

Nancy Li[a,1], D. Kwabena Bediako[a,1], Ryan G. Hadt[b], Dugan Hayes[b], Thomas J. Kempa[a], Felix von Cube[c], David C. Bell[c], Lin X. Chen[b,d], and Daniel G. Nocera[a,2]

[a]Department of Chemistry and Chemical Biology, Harvard University, Cambridge, MA 02138; [b]Chemical Sciences and Engineering Division, Argonne National Laboratory, Lemont, IL 60439; [c]Center for Nanoscale Systems, Harvard University, Cambridge, MA 02138; and [d]Department of Chemistry, Northwestern University, Evanston, IL 60208

Contributed by Daniel G. Nocera, December 19, 2016 (sent for review July 12, 2016; reviewed by Curtis P. Berlinguette and Shannon W. Boettcher)

Iron doping of nickel oxide films results in enhanced activity for promoting the oxygen evolution reaction (OER). Whereas this enhanced activity has been ascribed to a unique iron site within the nickel oxide matrix, we show here that Fe doping influences the Ni valency. The percent of Fe^{3+} doping promotes the formation of formal Ni^{4+}, which in turn directly correlates with an enhanced activity of the catalyst in promoting OER. The role of Fe^{3+} is consistent with its behavior as a superior Lewis acid.

water splitting | renewable energy | electrocatalysis | oxygen evolution reaction | catalysis

Increasing the solar-to-fuels conversion efficiency of artificial photosynthetic systems relies on continued improvements in understanding the chemistry of catalytic water splitting, especially the oxygen evolution reaction (OER) (1–3). It is known since the studies of Corrigan in the 1980s that oxidic Ni thin films with trace Fe content exhibit exceptional OER activity (4–8). The behavior of Fe-doped Ni (Fe:Ni) oxide films under basic conditions (1 M KOH) has been revisited (9–19) and in this recent body of work, the role of Fe in these films has come under debate. X-ray absorption spectra of Fe:Ni oxide films supported by computational studies have led to the contention that Fe^{3+} species are the active sites for water oxidation (13). The conductivity of the metal (Ni and Co) oxido framework has been observed to increase with Fe content, with the oxide also potentially serving as a scaffold for Fe active sites (16, 17). Interestingly, unary Fe oxide films, however, are inferior OER catalysts. Whereas iron oxide displays modest intrinsic activity at high overpotentials ($\eta > 350$ mV) (17), at low overpotentials ($\eta <$ 300 mV) the activity of the films is poor (17, 18, 20–22), even as ultrathin submonolayer films (22). Interestingly, the Tafel slope of Fe:Ni oxido films changes with increasing Fe content (7). Based on the reaction–diffusion behavior of multilayer oxygen evolving catalyst (OEC) films (23), Fe centers as isolated (i.e., noninteracting) sites embedded in a conductive matrix may be expected to alter the exchange current density with Fe content but not necessarily the Tafel slope. In contradistinction to an Fe active site model for Fe:Ni oxides, although Mössbauer studies of Fe:Ni layered double hydroxides provide direct evidence for the formation of Fe^{4+} in Fe:Ni oxide catalysts during OER, these Fe^{4+} sites do not account for the observed catalytic activity (24). Moreover, the formed "active oxygen" species have been found to be adsorbed on nickel sites in Fe:Ni films in borate buffer (25–27), suggesting Ni centers as active sites for OER. These results together suggest that the presence of Fe active sites may not be the primary reason for the enhanced activity of Fe:Ni catalysts films and point to another chemical role for Fe in oxidic Ni films.

Fe:Ni oxide films may be prepared by nitrate electroreduction, which creates a basic pH at the electrode resulting in rapid precipitation induced by local pH increases. Under these basic conditions, Fe oxide/hydroxide is prone to preferential deposition owing to differences in solubility product constants for $Ni(OH)_2$ versus $Fe(OH)_2$ ($K_{sp} = 5.5 \times 10^{-16}$ and 4.9×10^{-17}, respectively) (28). Segregation of Fe and Ni oxido subdomains would make it difficult to examine the role of Fe in films at a mechanistic level. In contrast, addition of Fe through incidental doping or the more gradual anodic deposition technique is a more controlled deposition method that prevents rapid Fe precipitation. We have developed methods that permit metal oxido films to be anodically electrodeposited in a controlled fashion under near-neutral pH conditions where Fe precipitation is not prevalent (29–34). Oxidic Ni-based films may be deposited at intermediate pH by using borate (B_i) electrolyte and high activity from these NiB_i films may be achieved by anodic conditioning (31–33). In conjunction with these studies, electrochemical redox titrimetry and in situ (32) and ex situ (35) X-ray absorption spectroscopy (XAS) at the nickel K edge has revealed a correlation of the catalytic activation with a rise beyond 3 in the formal valence of the Ni resting state. Indeed, immediately following deposition, nickel centers persist as Ni^{3+} in a low-activity β-NiOOH-like phase; anodization results in oxidation to a mixed-valence $Ni^{3.6+}$ γ-NiOOH-like phase, which serves as the resting state for the active catalyst (32). These studies support the notion that the active Ni phase in NiOOH-mediated OER is the Ni^{4+}-containing γ-NiOOH phase. Taking into account the spectroscopic data demonstrating the correlation between activity and Ni^{4+} content (32), we have now interrogated the influence of Fe content on Ni valence by electrochemical redox titration of ultrathin (<10 nm) catalyst films, with additional characterization using Ni K-edge XAS and O K-edge electron energy loss spectroscopy (EELS). We show that the resting state

Significance

Iron-doped nickel oxide films are the most active nonnoble metal oxygen evolution reaction (OER) catalysts in alkaline electrolyte. Since Corrigan's original discovery of enhanced activity with Fe doping in nickel oxides, the chemical basis for this synergy remains unclear. Recent studies suggest iron to assume a high valent oxidation state, thus promoting OER. We provide evidence for an alternative role of Fe^{3+} as a Lewis acid in the host nickel oxide. We observe that Fe^{3+} promotes the formation of Ni^{4+}, which leads to enhanced catalytic activity. This result is consistent with Fe^{3+} to be one of the strongest Lewis acidic metals by any measure of Lewis acidity, including hard–soft acid base theory, metal ion pK_as, and chemical inertness.

Author contributions: N.L., D.K.B., R.G.H., D.C.B., L.X.C., and D.G.N. designed research; N.L., D.K.B., R.G.H., D.H., T.J.K., and F.v.C. performed research; N.L., D.K.B., and R.G.H. contributed new reagents/analytic tools; N.L., D.K.B., R.G.H., D.H., and D.G.N. analyzed data; and N.L., D.K.B., R.G.H., and D.G.N. wrote the paper.

Reviewers: C.P.B., University of British Columbia; and S.W.B., University of Oregon.

The authors declare no conflict of interest.

[1]N.L. and D.K.B. contributed equally to this work.

[2]To whom correspondence should be addressed. Email: dnocera@fas.harvard.edu.

This article contains supporting information online at www.pnas.org/lookup/suppl/doi:10.1073/pnas.1620787114/-/DCSupplemental.

Table 1. Summary of film preparation, analysis, and Fe content

Entry	Film	Fe incorporation method	Film preparation*	Fe content, mol %†
			NiB_i films	
1	NiB_i	None	As-deposited	1.04 ± 0.46
2	NiB_i	None	Anodized in Fe-free solution (1 M KOH)	1.60 ± 0.38
3	NiB_i	None	Anodized in Fe-free solution (1 M KB_i pH 9.2)	0.58
			Fe:NiB_i films from trace Fe incorporation	
4	Fe^{tr}:NiB_i	Incubate in reagent grade 1 M KB_i pH 9.2	Anodized in Fe-free solution (1 M KOH)	2.91 ± 0.74–4.75 ± 1.87#
5	Fe^{tr}:NiB_i	Incubated in reagent grade 1 M KB_i pH 9.2	Anodized in Fe-free solution (1 M KB_i pH 9.2)	2.66–6.45#
6	Fe^{tr}:NiB_i	Anodized in reagent grade buffer	Anodized in reagent grade solution (1 M KOH)	11.43 ± 1.55
7	Fe^{tr}:NiB_i	Anodized in reagent grade buffer	Anodized in reagent grade solution (1 M KB_i pH 9.2)	27.34 ± 3.51
			Fe:NiB_i films from intentional Fe incorporation	
8	Fe^{cod}:NiB_i	None	As-deposited	4.47 ± 0.59
9	Fe^{cod}:NiB_i	Codeposition from Ni/Fe solution	Anodized in Fe-free solution (1 M KOH)	4.90 ± 0.64

*Electrodeposited films studied with no applied anodic preconditioning are designated as-deposited; electrodeposited films obtained from applying an anodic potential for 3 h either at 0.75 V vs. NHE in 1 M KOH or 1.15 V in 1 M KBi pH 9.2. are designated as anodized.
†Fe concentration determined from ICP-MS of dissolved films.
#Incubation times from 5 to 30 min.

of the Ni valence in these materials increases with Fe content to 10%, after which increased Fe content does not affect the Ni valency. Our results point to the role of Fe as a Lewis acid to increase the Ni valency, which in turn leads to the increase in OER activity of Fe-doped Ni oxido films.

Results and Discussion

Table 1 lists the three types of NiB_i films examined in this study: pure NiB_i films with no Fe, and NiB_i films with Fe incorporation either from trace Fe (11, 14, 15) in reagent-grade KOH and B_i electrolytes (i.e., Fe^{tr}:NiB_i) or from Fe codeposited (14) from a known solution concentration (i.e., Fe^{cod}:NiB_i). Electrolyte solutions for the preparation of authentic NiB_i films must be either scrubbed of Fe in very basic pH conditions by subjecting the solutions to treatment with solid $Ni(OH)_2$ as previously described (11, 14) or cleaned by chelating resin complex in more neutral pH conditions as previously described (36) (see *SI Appendix* for details). Table 1 also lists different methods of film treatment. Films were studied either directly upon electrodeposition (designated as-deposited) or after holding the film at an anodic potential for 3 h either at 0.75 V in 1 M KOH or 1.15 V in 1 M KB_i pH 9.2 (designated anodized). All potentials are in reference to the normal hydrogen electrode (NHE).

As-deposited and KOH-anodized NiB_i films (entries 1 and 2 in Table 1, entries 1–1 and 1–2, respectively) exhibit Fe content and OER activity similar to previous reports (14, 31–33). Ni and Fe metal ion concentrations were determined by inductively coupled plasma-mass spectrometry (ICP-MS) on solutions of digested films (rinsed in type I water) in ultrapure (doubly distilled) 2% nitric acid. All glassware was thoroughly acid-washed before use. The detection of Fe in as-deposited NiB_i films (Table 1, entry 1–1) at a level of 1.04 ± 0.46% and for films anodized in scrubbed electrolyte (Table 1, entry 1–2) at a level of 1.60 ± 0.38% is likely due to remnant trace Fe in glassware and the general experimental setup. As noted previously (14, 31–33), the OER activity of as-deposited NiB_i films in Fe-scrubbed electrolyte (Table 1, entry 1–1) is low (red trace, *SI Appendix*, Fig. S1), consistent with the high Tafel slopes (90–100 mV/decade) characteristic of such films (14, 31–33). That the OER current density (j) does not vary over time suggests that an anodic potential alone does not modify NiB_i films operating in Fe-free media. Also consistent with previous results (14, 31–33), the operation of these as-deposited NiB_i films (Table 1, entry 1–1) in reagent-grade electrolyte (which contains adventitious amounts of Fe) shows a dramatic increase in activity (blue trace, *SI Appendix*, Fig. S1), attendant to a decreased Tafel slope of 30 mV/decade (33).

The valencies of Ni in these films (Table 1, entries 1–1 and 1–2) were electrochemically assessed by coulometric titration in Fe-free 1 M KOH. This measurement was also carried out on Fe^{tr}:NiB_i films (Table 1, entries 1–4, 1–6, and 1–7). Films ≤7 nm (a few monolayers) thick are obtained by terminating deposition upon the passage of 1.0 mC/cm^2 (32, 33). The use of such ultrathin films ensures that charge transport is not a predominant factor in evaluating film redox properties. The total charge passed in the electroreduction of Ni centers in NiB_i and Fe^{tr}:NiB_i films (blue trace, Fig. 1*A*) was determined from the cyclic voltammogram (red trace, Fig. 1*A*), permitting the total number of electrons consumed upon reduction to Ni^{2+} to be quantified.

Fig. 1*A* shows exemplary data for the cyclic voltammogram and current integration (charge) curve for NiB_i films anodized in Fe-free electrolyte (Table 1, entry 1–2). By determining the total Ni and Fe content in these films from ICP-MS analysis, the Ni valency may be calculated. For NiB_i films (Table 1, entry 1–2), we observe that 1.2 ± 0.1 electrons are consumed per Ni center, revealing that a Ni valency of +3.2(1) is sustained upon anodization

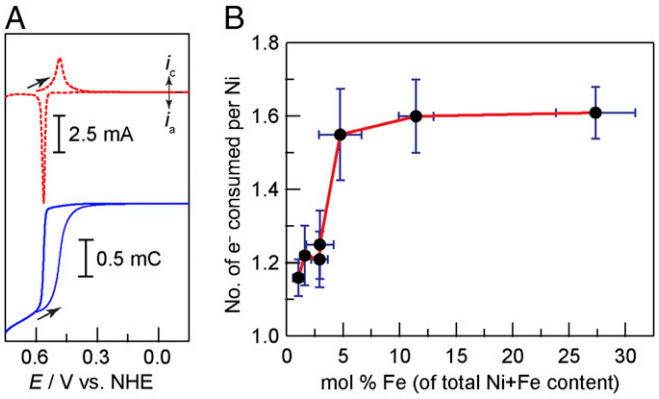

Fig. 1. (*A*) CV in Fe-free 1 M KOH of a NiB_i film deposited onto a fluorine-doped tin oxide (FTO)-coated glass slide and anodized for 3 h in Fe-free 1.0 M KOH (Table 1, entry 1–2). Scan rate: 0.1 V/s. Current (top, dashed line) and total charge (bottom, solid line) data are offset for clarity. (*B*) Plot of coulometric titration data against the Fe content for NiB_i and Fe^{tr}:NiB_i films in the as-deposited (Table 1, entry 1–1) and reagent-grade anodized states (Table 1, entries 1–6 and 1–7), as well as upon anodization in Fe-free KOH following exposure to reagent-grade 1 M KB_i electrolyte for 0, 5, 10, or 30 min (Table 1, entries 1–2 and 1–4). Error bars derived from three independent measurements.

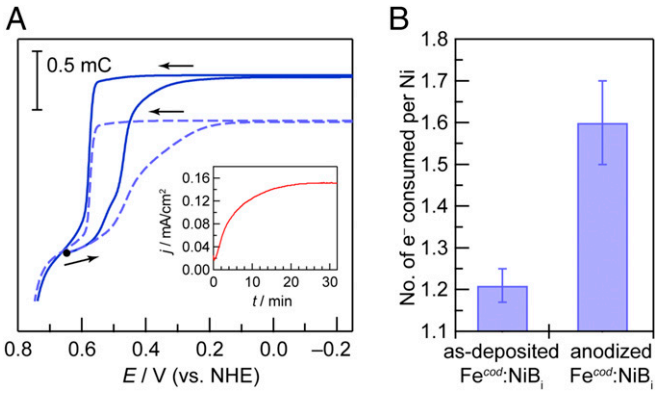

Fig. 2. Fe^{cod}:NiB_i films deposited in the presence of Fe^{3+}. (*A*) Coulometric titration of as-deposited (Table 1, entry 1–8) (blue, dashed line) and anodized (Table 1, entry 1–9) (dark blue, solid line) films showing a significantly greater amount of charge passed following anodization. The dot marks the start of the scan and arrows show scan direction. (*Inset*) Chronoamperometric trace over the course of anodization at 0.75 V in Fe-free 1 M KOH showing activation. (*B*) Coulometric titration data for codeposited Fe:Ni oxide films (Table 1, entries 1–8 and 1–9).

in Fe-free solution. A similar result of 1.16 ± 0.05 e^-/Ni (Ni valency of +3.2) is also obtained for films in the as-deposited state (Table 1, entry 1–1), matching previous values for as-deposited NiB_i films (32). Our analysis assumes that Fe^{4+} sites, if present (as has been reported for a 3:1 Ni:Fe layered double hydroxide, LDH) (24), do not consume electrons to produce Fe^{3+} sites. Indeed, at most, 1/5 of the Fe sites in these LDHs are Fe^{4+}; with this benchmark, even if all of the iron content in NiB_i films were reduced to Fe^{3+}, this would account for negligible electron consumption given our low Fe content (under 5% for Fe incorporated through incubation, *vide infra*). We note that integration of the cathodic wave is more reliable than integrating the corresponding anodic wave of the $Ni^{3+/2+}$ redox feature (*SI Appendix*, Fig. S2). As shown by *SI Appendix*, Fig. S2*B*, the integrated charge curve for cyclic voltammogram (CV) scans recorded toward reductive potentials is defined clearly by an extended plateau where the film has been completely reduced to Ni^{2+}. This is not the case for integration of the anodic feature, which merges into the OER wave. This likely explains the observation of Corrigan and Bendert (8) and Merrill et al. (37) that NiB_i in the absence of significant Fe incorporation exhibits a redox level of 1.6 e^-/Ni above Ni^{2+}. In these measurements, the Ni valency was determined from the anodic wave of the $Ni^{3+/2+}$ redox feature where contributions of OER to the measured current would lead to inflated values in the Ni redox level. Furthermore, we note that the films used by Corrigan were much thicker than reported here (~470 nm versus ~7 nm based on average Ni loading comparison). In thick films, a CV sweep conducted for coulometric analysis may not capture all Ni center reductions because of poor electron transfer as the film is made increasingly insulating by Ni^{2+} centers during the reduction. We avoid this issue by using ultrathin films to ensure that the entirety of the film is subject to interrogation by redox titrimetry. We also note that different materials and conditions lead to different values of Ni valency. Smith and Berlinguette have observed 4 e^-/Ni transferred for photochemically prepared α-NiO_x films upon integration of the first anodic peak (38), although with repeated cycling of the film, the e^-/Ni calculated with subsequent cycling converges to ~1.2 e^- per Ni, as we observe here. Studies of other NiFe-based LDHs show a trend in decreased Ni valency with increasing Fe (39) which may be explained by a different resting state species such as a NiFe hydroperoxide (40). Also of note, at high iron concentrations, phase-segregated Fe hydroxide phases may be prevalent and thus could complicate accurate measurements of Ni valency.

NiB_i films were doped with increasing quantities of Fe by incubating the as-deposited films in reagent-grade 1 M KB_i pH 9.2 electrolyte (that had not been subject to the Fe scrubbing procedure) at open circuit for varying times (5, 10, 30 min) and subsequently anodized in Fe-free KOH (Table 1, entry 1–4). The amount of iron incorporated into these films increases steadily with incubation time (*SI Appendix*, Fig. S3) as the onset potential to OER decreases (*SI Appendix*, Fig. S2*A*). Incorporation of Fe via this incubation method is advantageous because it allows us to resolve the behavior of uniform films with low Fe content (<5 mol %). Fig. 1*B* plots the coulometric titration data versus the percentage of Fe doping for films prepared by this incubation process (Table 1, entry 1–4) along with that obtained from films prepared by the aforementioned methods (Table 1, entries 1–1, 1–2, 1–6, and 1–7). The maximal mixed-valence resting state of $Ni^{3.6+}$ is achieved at Fe doping levels of 4%, and beyond a doping level of 10% Fe, there is no further increase in average Ni valence. Interestingly, the plateau at ≥10% Fe content observed here matches previous reports of maximal film activity at ~10% Fe doping (10, 13, 15, 18). Moreover, the $Ni^{3.6+}$ value matches that previously measured for NiB_i films anodized in reagent-grade 1 M KB_i buffer (33), which likely contains Fe as a contaminant on par with the highest Fe content in Fe^{tr}:NiB_i (Table 1, entry 1–7) measured here (*SI Appendix*, Fig. S3). This plateau in Ni valence with Fe content again emphasizes that electrons consumed during coulometric titrations are going toward reduction of higher valence nickel centers to Ni^{2+} as opposed to the reduction of Fe^{4+} to Fe^{3+}.

To distinguish the role of increasing Fe content during an applied anodic potential, coulometric titration/ICP-MS analysis was conducted on films prepared by codeposition of Ni and Fe (Fe^{cod}:NiB_i) in the as-deposited and anodized state (Table 1, entries 1–8 and 1–9, respectively). Here, we followed previously published (14) procedures to anodically electrodeposit ultrathin films (deposition charge of 1.0 mC/cm^2) from a pH 9.2 KB_i electrolyte containing a 9:1 molar ratio of Ni^{2+} and Fe^{2+}. Table 1, film entry 1–8 shows a steady increase in activity with a plateau after 1 h (Fig. 2*A*, *Inset*), similar to that observed upon anodization of NiB_i films in reagent-grade electrolyte (*SI Appendix*, Fig. S1, blue trace) (33, 34). Redox titrimetry followed by elemental analysis of digested films reveals that the average Ni valence in these Fe^{cod}:NiB_i films increases over the course of the electrochemical activation from +3.21(4) (as-deposited, Table 1, entry 1–8) to +3.6(1) (anodized, Table 1, entry 1–9) as shown in

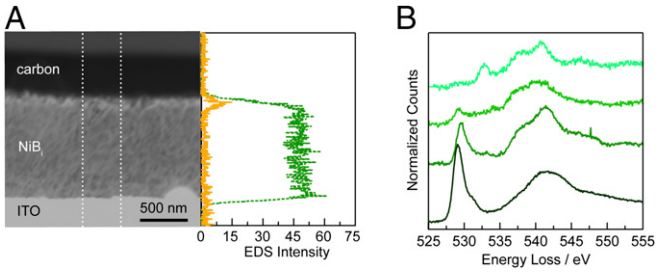

Fig. 3. (*A*, *Left*) Dark-field STEM image of a typical cross-sectioned catalyst film sample showing: a portion of the indium tin oxide (ITO) substrate, the Fe^{tr}:NiB_i (Table 1, entry 1–7) catalyst layer (anodized in reagent-grade KB_i electrolyte), and protective carbon overcoats applied before focused ion beam milling. (*Right*) Energy-dispersive X-ray spectroscopy (EDS) elemental profile (Ni: green; Fe: orange) with EDS counts summed across the region between the dotted lines. (*B*) Oxygen K-edge EELS of nickel oxide model compounds. From top to bottom: $Ni^{II}O$, $Ni^{II}(OH)_2$, $LiNi^{III}O_2$, and γ-$Ni^{III/IV}OOH$. Spectra were normalized to the edge jump and offset for clarity.

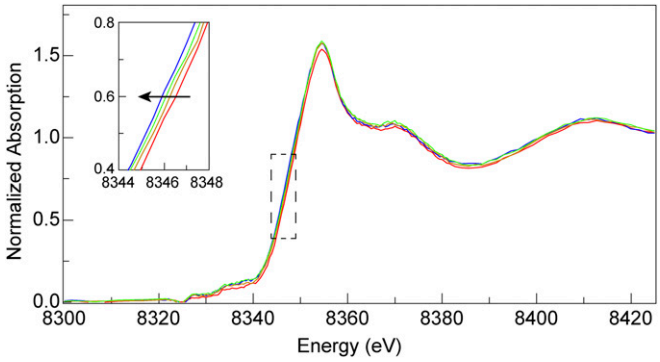

Fig. 4. Ni K-edge XANES spectra of reagent-grade 1 M KB_i pH 9.2 anodized Fe^{tr}:NiB_i film (12.30 mol % Fe) (Table 1, entry 1–7) (blue), as well as Fe^{tr}:NiB_i films anodized in Fe-free 1 M KB_i pH 9.2 following exposure to reagent-grade 1 M KB_i electrolyte for 0 (red), 15 (orange), or 25 (green) min to obtain Fe content of 0.58, 2.66, and 6.45 mol % Fe, respectively (Table 1, entries 1–3 and 1–5). (*Inset*) Zoomed-in K-edge shift of spectra as indicated by dotted box in *A*. All films were poised at 1.3 V during anodization and XAS scans.

Fig. 2*B*. This result agrees with previous work that shows anodization results in significant increase in turnover frequency even for codeposited Fe^{cod}:NiB_i films (14).

The results of Figs. 1 and 2 show that the presence of Fe alone does not promote the formation of higher valent Ni species. Instead, the combination of Fe and electrochemical polarization at moderately high potentials (anodization) is necessary for activation. Previous XAS studies show that anodization drives a phase change from β-NiOOH (valency 3.2) to γ-NiOOH (valency 3.6) (32). Fe dopants make this phase transition more accessible but Fe incorporation alone cannot achieve this transformation. That the presence of Fe facilitates the formation of Ni^{4+} to yield an overall average $Ni^{3.6+}$ formal oxidation of the resting state suggests that Fe dopants make this phase transition more accessible. It remains undefined if Fe increases Ni valency to drive the structural change or vice versa.

To study the difference between anodized Fe:NiB_i films formed from codeposition (Fe^{cod}:NiB_i, Table 1, entry 1–9) versus incidental doping (Fe^{tr}:NiB_i, Table 1, entry 1–7), we conducted cross-sectional elemental analysis of a thick NiB_i catalyst film (~1 μm) that was anodized in reagent-grade KB_i pH 9.2 electrolyte (Table 1, entry 1–7). The results reveal an anisotropic distribution of Fe in the film with the predominant localization of Fe in the outermost ~100 nm of the catalyst film (Fig. 3*A*). Similarly, thick as-deposited films that were not subjected to anodization (Table 1, entry 1–1) do not display significant Fe counts across the film (*SI Appendix*, Fig. S4). This result again emphasizes the need to make measurements of Ni valency on thin films, as performed in our studies here. Importantly, this result also offers insight into the possible origin of the apparently higher activity observed upon codeposition of Fe^{cod}:NiB_i in thicker films (14). Codeposition gives rise to a more homogeneous distribution of Fe throughout a thick film. Consequently, a greater proportion of the Ni centers throughout a thick film would attain a Ni^{4+} valency upon anodization, resulting in higher activity.

To investigate why greater Ni^{4+} valence is beneficial to greater catalytic OER activity, we probed the influence of formal Ni valence on the electronic structure of oxygen ions in Ni oxide models (Fig. 3*B*). Oxygen K-edge spectroscopy largely probes transitions between O 1*s* and unoccupied metal orbitals (i.e., 3*d*, and 4*s*/4*p*). Such spectra typically feature a preedge feature centered at ~530 eV and a broader set of overlapping bands spanning the 535–550-eV range. The preedge results from transitions to unoccupied metal 3*d* orbitals that are hybridized with O 2*p* character (formally a $1s \rightarrow 3d$ transition that gains dipole allowed intensity via O 2*p* mixing).

Spectral intensity above the preedge is associated with states that have O 2*p* character hybridized with unoccupied metal 4*s* and 4*p* orbitals (41–43). The intensity of the preedge has been shown to be a powerful measure of the covalency of metal–oxygen bonds (41). As shown in Fig. 3*B*, EELS (see *SI Appendix* for details) of a series of model Ni oxide compounds reveals a pronounced increase in the intensity of the preedge feature as the formal oxidation state of Ni increases from NiO to γ-NiOOH. These data indicate increased covalency in Ni–O bonding as the formal Ni oxidation state is increased. As a direct consequence of the electronic considerations embodied by the "Oxo Wall" (44), the formal oxidation state of Ni(IV)–oxo (Ni(IV) ⩵ O) will possess significant Ni(III)–$O^{\bullet}$ resonance character with increased covalency. Such oxyl radical character is consistent with increasing evidence for the role of oxygen radicals in O–O bond formation by a proton-coupled electron transfer (PCET) mechanism involving water (45–47), most likely to generate a hydroperoxide intermediate from which oxygen is generated (48). To this end, increased Ni^{4+} generation by Fe incorporation will lead to greater Ni–O covalency, and thus greater oxyl character, which can manifest in increased OER activity.

XAS of Ni centers in NiB_i during OER also show increased Ni–O covalency as Fe loading is increased. The in situ X-ray absorption near-edge spectra data are given in Fig. 4 for anodized NiB_i (Table 1, entry 1–3) and Fe^{tr}:NiB_i films (Table 1, entry 1–5 and entry 1–7). A systematic red-shift of the Ni K edge is observed upon increased Fe incorporation from 0.58 mol % to 12.30 mol % Fe. The magnitude of this edge shift (−0.8 eV) is less than that associated with reducing $Ni^{3+/4+}$ in the anodized

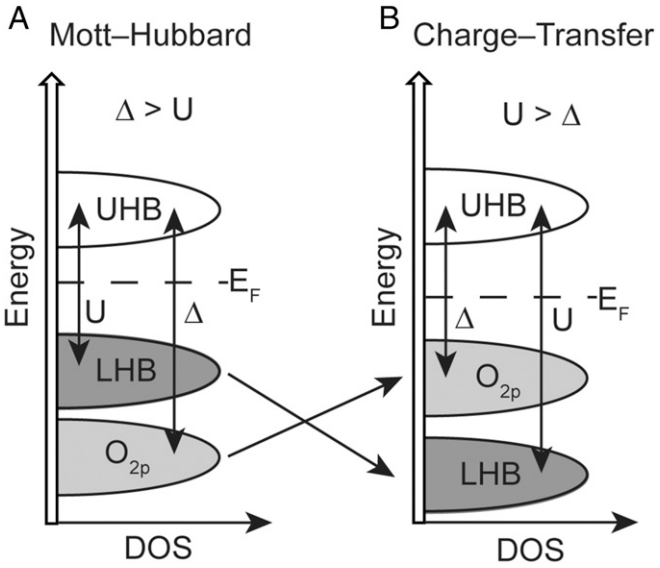

Fig. 5. Schematic energy-band vs. density of states (DOS) diagrams of (*A*) a Mott–Hubbard insulator and (*B*) a charge-transfer insulator. The occupied O 2*p* bands are shaded in light gray whereas the metal *d* bands are shaded in dark gray for occupied bands and unshaded for unoccupied bands. The unoccupied and occupied *d* bands are represented by the UHB and LHB, respectively. The *d*-*d* coulomb and exchange energy transfer (U) between UHB and LHB of the metal *d* bands and the *p*-to-*d* charge-transfer energy (Δ) terms are also indicated. The Fermi energy (E_F) level is indicated by the dotted dashed line. Mott–Hubbard insulators and charge-transfer insulators are differentiated by their relative values of U versus Δ to result in the highest occupied band being either metal or ligand character, which in turn results in either metal oxidation (Mott–Hubbard insulator) or ligand oxygen oxidation (charge-transfer insulator), respectively.

film to Ni^{2+} (*SI Appendix*, Fig. S5). Additionally, the edge shift upon Fe incorporation is less than that previously observed (40, 49) with the caveats that the results of Fig. 4 have been obtained under OER conditions with less Fe incorporation. If X-ray–induced photoreduction were to give rise to this <1-eV change in edge energy (50, 51), we would expect a systematic, instantaneous photoreduction across the different films. However, spectral changes do not change over multiple scans, suggesting that photoreduction of the film is not occurring upon continuous X-ray exposure. On the other hand, it is well established that the Ni K edge is sensitive to changes in oxidation and spin state as well as ligand–metal covalency. Increased Ni–O covalency results in a decreased effective nuclear charge, Z_{eff}, of the metal, which in turn results in a red-shift of the edge transition(s) (i.e., $1s \rightarrow 4p$). Additionally, increased metal–ligand covalency can result in a broadening and increased intensity of the edge transitions due to delocalization of the metal 4*p* orbitals (52). Our observations are also in line with comparative Ni K-edge X-ray absorption near edge structure (XANES) spectra of Ni/Mn molecular complexes with hard O, N-donor and soft Cl, S-donor ligands, which show that the edge energy shifts to lower energy with increased Ni–ligand covalency (52–54). Thus, the Ni K-edge data corroborate the O K-edge data of Fig. 3*B*—an increase in Fe loading results in an increase in Ni–O covalency.

The contributions of Ni(IV) $\doteqdot$ O versus Ni(III)–$O^{\bullet}$ resonances with covalency can be understood within the context of a Zaanen–Sawatzky–Allen scheme. In this treatment, transition-metal compounds may be classified as either Mott–Hubbard or charge-transfer insulators (55, 56). The electronic structure for these two regimes is determined by the relative values of U and Δ (57), where U is related to the *d-d* Coulomb and exchange interactions resulting from d_i^n, $d_j^n \leftrightarrow d_i^{n-1}$, d_j^{n+1} (i and j are electrons on neighboring metals) charge fluctuations, and Δ is related to the ionization energy of the ligand and electron affinity of the metal, and is therefore related to the ligand-to-metal charge-transfer (LMCT) energy ($d_i^n \rightarrow d_i^{n+1}L$, where the electron-hole is located on the ligand) (56). The relative values of U and Δ tune the metal–ligand character of the highest occupied band, which results in metal versus oxide oxidation (Fig. 5). For large Δ (Δ > U), the oxygen valence band lies below the occupied *d*-orbital band [i.e., lower Hubbard band (LHB)], giving rise to a Mott–Hubbard-type insulator, as depicted in Fig. 5. Conversely, for small Δ (U > Δ), the oxygen valence band lies above the occupied d-orbital band, giving rise to a charge-transfer-type insulator. The relative values of U and Δ are determinants of the Ni(IV) $\doteqdot$ O ↔ Ni(III)–$O^{\bullet}$ resonance structures. Decreasing Δ (more covalent interaction due to greater ligand–metal orbital mixing) and increasing U will favor covalency and hence a greater Ni(III)–$O^{\bullet}$ resonance contribution (owing to the ordering of the O_{2p} band above LHB). This model is consistent with our results of a greater Ni–O covalency arising from a higher effective formal oxidation state of Ni with Fe doping. The result is also consistent with the observation of increased conductivity of the Ni oxide lattice with Fe doping (11) inasmuch as a decrease in Δ and increase in U induces more charge-transfer character within the lattice.

Conclusions

The ability to access the Ni^{4+} in the resting state of Ni oxido OECs at modest overpotentials (η ~ 350–250 mV) is directly correlated to the presence of Fe in NiB_i films. Coulometric titration results reveal that the resting state valency of Ni increases by 0.5 for Fe loadings of 5–10%. Attendant to this increase in Ni valency, O and Ni K-edge spectra reveal a greater Ni–O covalency. On the basis of the studies reported herein, the role of Fe in promoting the OER at nickel oxide catalysts appears in large part to be a Lewis acid effect. By any measure, Fe^{3+} is strong Lewis acid. The chemical hardness scale of Parr et al. places Fe^{3+} as one of the "hardest" ions in the periodic table (58, 59), which is also supported by the less quantitative predictions of hard–soft acid–base theory (60). Within the context of the study herein, a very relevant measure of the Lewis acidity is offered by the pK_a of the hexaqua metal complex. Computation and experiment show Fe^{3+} to be the most acidic transition metal ion with a $pK_a = 2.2$ for the deprotonation of coordinated water (61). Accordingly, the incorporation of the Lewis acid Fe^{3+} into Ni oxido catalyst clusters would serve to increase the acidity of OH_x (aqua/hydroxo) moieties that are coordinated to nickel, thereby lowering the reduction potential for the $Ni^{4+/3+}$ couple and thus engendering a greater population of Ni^{4+} in the Fe-doped catalysts. This in turn leads to greater oxyl character arising from the Ni(IV) $\doteqdot$ O ↔ Ni(III)–$O^{\bullet}$ resonance contribution. In light of the recognized role of the oxyl radical in promoting O–O bond formation via PCET (62–69), the role of Fe^{3+} in NiB_i to promote increased oxyl character is of beneficial consequence to increasing OER activity in metal oxidic catalyst films.

ACKNOWLEDGMENTS. We are grateful to Adam Graham for assistance with scanning transmission electron microscopy (STEM), Zhongxing Chen for assistance with ICP, and Michael Huynh for helpful discussions. We also acknowledge Tianpin Wu, Lu Ma, and George Sterbinsky for assistance with XAS measurements. This material is based upon work supported under the Solar Photochemistry Program of the Chemical Sciences, Geosciences, and Biosciences Division, Office of Basic Energy Sciences of the US Department of Energy. R.G.H. is an Enrico Fermi Fellow at Argonne National Laboratory (ANL). D.H. is supported by the Joseph J. Katz Postdoctoral Fellowship at ANL. Work by D.C.B. and F.v.C. was supported by the Science and Technology Center for Integrated Quantum Materials, National Science Foundation (NSF) Grant DMR-1231319. Use of beamline 9BM-B at the Advanced Photon Source at ANL was supported by the US Department of Energy, Office of Science, Office of Basic Energy Sciences, under Contract DE-AC02-06CH11357. The Center for Nanoscale Systems at Harvard University is a member of the National Nanotechnology Infrastructure Network, which is supported by the National Science Foundation under ECS-0335765.

1. Lewis NS, Nocera DG (2006) Powering the planet: chemical challenges in solar energy utilization. *Proc Natl Acad Sci USA* 103(43):15729–15735.
2. Lewis NS, Nocera DG (2015) The solar opportunity. *The Bridge* 46:41–47.
3. Cook TR, et al. (2010) Solar energy supply and storage for the legacy and nonlegacy worlds. *Chem Rev* 110(11):6474–6502.
4. Conway BE, Bourgault PL (1959) The electrochemical behavior of the nickel–nickel oxide electrode: Part I. Kinetics of self-discharge. *Can J Chem* 37:292–307.
5. Lu PW, Srinivasan S (1978) Electrochemical-ellipsometric studies of oxide film formed on nickel during oxygen evolution. *J Electrochem Soc* 125:1416–1422.
6. Bockris JO'M, Otagawa T (1983) Mechanism of oxygen evolution on perovskites. *J Phys Chem* 87:2960–2971.
7. Corrigan DA (1987) The catalysis of the oxygen evolution reaction by iron impurities in thin film nickel oxide electrodes. *J Electrochem Soc* 134:377–384.
8. Corrigan DA, Bendert RM (1989) Effect of coprecipitated metal ions on the electrochemistry of nickel hydroxide thin films: Cyclic voltammetry in 1M KOH. *J Electrochem Soc* 136:723–728.
9. Trotochaud L, Ranney JK, Williams KN, Boettcher SW (2012) Solution-cast metal oxide thin film electrocatalysts for oxygen evolution. *J Am Chem Soc* 134(41):17253–17261.
10. Louie MW, Bell AT (2013) An investigation of thin-film Ni-Fe oxide catalysts for the electrochemical evolution of oxygen. *J Am Chem Soc* 135(33):12329–12337.
11. Trotochaud L, Young SL, Ranney JK, Boettcher SW (2014) Nickel-iron oxyhydroxide oxygen-evolution electrocatalysts: The role of intentional and incidental iron incorporation. *J Am Chem Soc* 136(18):6744–6753.
12. Hunter BM, et al. (2014) Highly active mixed-metal nanosheet water oxidation catalysts made by pulsed-laser ablation in liquids. *J Am Chem Soc* 136(38):13118–13121.
13. Friebel D, et al. (2015) Identification of highly active Fe sites in (Ni,Fe)OOH for electrocatalytic water splitting. *J Am Chem Soc* 137(3):1305–1313.
14. Smith AM, Trotochaud L, Burke MS, Boettcher SW (2015) Contributions to activity enhancement via Fe incorporation in Ni-(oxy)hydroxide/borate catalysts for near-neutral pH oxygen evolution. *Chem Commun (Camb)* 51(25):5261–5263.
15. Klaus S, Cai Y, Louie MW, Trotochaud L, Bell AT (2015) Effects of Fe electrolyte impurities on $Ni(OH)_2$/NiOOH structure and oxygen evolution activity. *J Phys Chem C* 119:7243–7254.
16. Burke MS, Kast MG, Trotochaud L, Smith AM, Boettcher SW (2015) Cobalt-iron (oxy)hydroxide oxygen evolution electrocatalysts: The role of structure and composition on activity, stability, and mechanism. *J Am Chem Soc* 137(10):3638–3648.

17. Burke MS, et al. (2015) Revised oxygen evolution reaction activity trends for first-row transition-metal (oxy)hydroxides in alkaline media. *J Phys Chem Lett* 6(18): 3737–3742.
18. Swierk JR, Klaus S, Trotochaud L, Bell AT, Tilley TD (2015) Electrochemical study of the energetics of the oxygen evolution reaction at nickel iron (oxy)hydroxide catalysts. *J Phys Chem C* 119:19022–19029.
19. Ahn HS, Bard AJ (2016) Surface interrogation scanning electrochemical microscopy of $Ni_{1-x}Fe_xOOH$ ($0 < x < 0.27$) oxygen evolving catalyst: Kinetics of the "fast" iron sites. *J Am Chem Soc* 138(1):313–318.
20. Lyons MEG, Brandon MP (2008) The oxygen evolution reaction on passive oxide covered transition metal electrodes in alkaline solution. Part III – Iron. *Int J Electrochem Sci* 3:1463–1503.
21. Man IC, et al. (2011) Universality in oxygen evolution electrocatalysis on oxide surfaces. *ChemCatChem* 3:1159–1165.
22. Subbaraman R, et al. (2012) Trends in activity for the water electrolyser reactions on 3d M(Ni,Co,Fe,Mn) hydr(oxy)oxide catalysts. *Nat Mater* 11(6):550–557.
23. Bediako DK, Costentin C, Jones EC, Nocera DG, Savéant J-M (2013) Proton-electron transport and transfer in electrocatalytic films. Application to a cobalt-based O_2-evolution catalyst. *J Am Chem Soc* 135(28):10492–10502.
24. Chen JYC, et al. (2015) Operando analysis of NiFe and Fe oxyhydroxide electrocatalysts for water oxidation: Detection of Fe^{4+} by Mössbauer spectroscopy. *J Am Chem Soc* 137(48):15090–15093.
25. Trześniewski BJ, et al. (2015) In situ observation of active oxygen species in Fe-containing Ni-based oxygen evolution catalysts: The effect of pH on electrochemical activity. *J Am Chem Soc* 137(48):15112–15121.
26. Morales OD, Ferrus-Suspedra D, Koper MTM (2016) The importance of nickel oxyhydroxide deprotonation on its activity towards electrochemical water oxidation. *Chem Sci* 7:2639–2645.
27. Yoshida M, et al. (2015) Direct observation of active nickel oxide cluster in nickel–borate electrocatalyst for water oxidation by in situ O K–edge X–ray absorption spectroscopy. *J Phys Chem C* 119:19279–19286.
28. Lide, DR, ed (2003) CRC Handbook of Chemistry and Physics, ed Lide, DR (CRC Press, Boca Raton, FL), 84th Ed, Sect 8, No. 120–121.
29. Kanan MW, Nocera DG (2008) In situ formation of an oxygen-evolving catalyst in neutral water containing phosphate and Co^{2+}. *Science* 321(5892):1072–1075.
30. Surendranath Y, Dincă M, Nocera DG (2009) Electrolyte-dependent electrosynthesis and activity of cobalt-based water oxidation catalysts. *J Am Chem Soc* 131(7):2615–2620.
31. Dincă M, Surendranath Y, Nocera DG (2010) Nickel-borate oxygen-evolving catalyst that functions under benign conditions. *Proc Natl Acad Sci USA* 107(23):10337–10341.
32. Bediako DK, et al. (2012) Structure-activity correlations in a nickel-borate oxygen evolution catalyst. *J Am Chem Soc* 134(15):6801–6809.
33. Bediako DK, Surendranath Y, Nocera DG (2013) Mechanistic studies of the oxygen evolution reaction mediated by a nickel-borate thin film electrocatalyst. *J Am Chem Soc* 135(9):3662–3674.
34. Huynh M, Bediako DK, Nocera DG (2014) A functionally stable manganese oxide oxygen evolution catalyst in acid. *J Am Chem Soc* 136(16):6002–6010.
35. Risch M, et al. (2011) Nickel-oxido structure of a water-oxidizing catalyst film. *Chem Commun (Camb)* 47(43):11912–11914.
36. Wuttig A, Surendranath Y (2015) Impurity ion complexation enhances carbon dioxide reduction catalysis. *ACS Catal* 5:4479–4484.
37. Merrill M, Worsley M, Wittstock A, Biener J, Stadermann M (2014) Determination of the "NiOOH" charge and discharge mechanisms at ideal activity. *J Electroanal Chem* 717:177–188.
38. Smith RDL, Berlinguette CP (2016) Accounting for the dynamic oxidative behavior of nickel anodes. *J Am Chem Soc* 138(5):1561–1567.
39. Görlin M, et al. (2016) Oxygen evolution reaction dynamics, faradaic charge efficiency, and the active metal redox states of Ni-Fe oxide water splitting electrocatalysts. *J Am Chem Soc* 138(17):5603–5614.
40. Black JF (1978) Metal-catalyzed autoxidation. The unrecognized consequences of metal-hydroperoxide complex formation. *J Am Chem Soc* 100:527–535.
41. Grioni M, Fuggle JC, Ghijsen J, Sawatzky GA, Petersen H, de Groot FM (1989) Oxygen 1s x-ray-absorption edges of transition-metal oxides. *Phys Rev B Condens Matter* 40(8):5715–5723.
42. Kuiper P, Kruizinga G, Ghijsen J, Sawatzky GA, Verweij H (1989) Character of holes in $Li_xNi_{1-x}O$ and their magnetic behavior. *Phys Rev Lett* 62(2):221–224.
43. Yoon W-S, Chung KY, McBreen J, Fischer DA, Yang X-Q (2006) Changes in electronic structure of the electrochemically Li-ion deintercalated $LiNiO_2$ system investigated by soft X-ray absorption spectroscopy. *J Power Sources* 163:234–237.
44. Winkler J, Gray H (2012) Electronic structures of oxo-metal ions. *Molecular Electronic Structures of Transition Metal Complexes I, Structure and Bonding*, eds Mingos DMP, Day P, Dahl JP (Springer, Berlin), Vol 142, pp 17–28.
45. Wang L-P, Troy VV (2011) Direct-coupling O_2 bond forming a pathway in cobalt oxide water oxidation catalysts. *J Phys Chem Lett* 2:2200–2204.
46. Yang X, Baik MH (2006) *cis,cis*-$[(bpy)_2Ru^{V}O]_2O^{4+}$ catalyzes water oxidation formally via in situ generation of radicaloid Ru^{IV}–O*. *J Am Chem Soc* 128(23):7476–7485.
47. Jiang Y, et al. (2013) Promoting the activity of catalysts for the oxidation of water with bridged dinuclear ruthenium complexes. *Angew Chem Int Ed Engl* 52(12): 3398–3401.
48. Zhang M, de Respinis M, Frei H (2014) Time-resolved observations of water oxidation intermediates on a cobalt oxide nanoparticle catalyst. *Nat Chem* 6(4):362–367.
49. Bates MK, Jia Q, Doan H, Liang W, Mukerjee S (2016) Charge-transfer effects in Ni–Fe and Ni–Fe–Co mixed-metal oxides for the alkaline oxygen evolution reaction. *ACS Catal* 6:155–161.
50. Dubois L, Jacquamet L, Pécaut J, Latour J-M (2006) X-ray photoreduction of a di(μ-oxo)$Mn^{III}Mn^{IV}$ complex occurs at temperatures as low as 20 K. *Chem Commun (Camb)* 43(43):4521–4523.
51. Yi J, Orville AM, Skinner JM, Skinner MJ, Richter-Addo GB (2010) Synchrotron X-ray-induced photoreduction of ferric myoglobin nitrite crystals gives the ferrous derivative with retention of the O-bonded nitrite ligand. *Biochemistry* 49(29):5969–5971.
52. Sarangi R (2013) X-ray absorption near-edge spectroscopy in bioinorganic chemistry: Application to M-O_2 systems. *Coord Chem Rev* 257(2):459–472.
53. Penner-Hahn JE, et al. (1990) Structural characterization of the manganese sites in the photosynthetic oxygen-evolving complex using x-ray absorption spectroscopy. *J Am Chem Soc* 112:2549–2557.
54. Colpas GJ, et al. (1991) X-ray spectroscopic studies of nickel complexes, with application to the structure of nickel sites in hydrogenases. *Inorg Chem* 30:920–928.
55. Zaanen J, Sawatzky GA, Allen JW (1985) Band gaps and electronic structure of transition-metal compounds. *Phys Rev Lett* 55(4):418–421.
56. Imada M, Fujimori A, Tokura Y (1998) Metal-insulator transitions. *Rev Mod Phys* 70(4): 1039–1263.
57. Greiner MT, Lu Z-H (2013) Thin-film metal oxides in organic semiconductor devices: Their electronic structures, work functions and interfaces. *NPG Asia Mater* 5:e55.
58. Parr RG, Pearson RG (1983) Absolute hardness: Companion parameter to absolute electronegativity. *J Am Chem Soc* 105:7512–7516.
59. Yang W, Parr RG (1985) Hardness, softness, and the Fukui function in the electronic theory of metals and catalysis. *Proc Natl Acad Sci USA* 82(20):6723–6726.
60. Pearson RG (1968) Hard and soft acids and bases, HSAB, part 1: Fundamental principles. *J Chem Educ* 45:581–587.
61. Jerome SV, Hughes TF, Friesner RA (2014) Accurate pKa prediction in first-row hexaaqua transition metal complexes using the B3LYP-DBLOC method. *J Phys Chem B* 118(28): 8008–8016.
62. Siegbahn PEM, Blomberg MRA (2010) Quantum chemical studies of proton-coupled electron transfer in metalloenzymes. *Chem Rev* 110(12):7040–7061.
63. Lundberg M, Siegbahn PEM (2004) Theoretical investigations of structure and mechanism of the oxygen-evolving complex in PSII. *Phys Chem Chem Phys* 6:4772–4780.
64. Siegbahn PEM (2013) Water oxidation mechanism in photosystem II, including oxidations, proton release pathways, O-O bond formation and O_2 release. *Biochim Biophys Acta* 1827(8-9):1003–1019.
65. Meyer TJ, Huynh MH, Thorp HH (2007) The possible role of proton-coupled electron transfer (PCET) in water oxidation by photosystem II. *Angew Chem Int Ed Engl* 46(28): 5284–5304.
66. Sproviero EM, Gascón JA, McEvoy JP, Brudvig GW, Batista VS (2008) A model of the oxygen-evolving center of photosystem II predicted by structural refinement based on EXAFS simulations. *J Am Chem Soc* 130(21):6728–6730.
67. Hull JF, et al. (2009) Highly active and robust Cp* iridium complexes for catalytic water oxidation. *J Am Chem Soc* 131(25):8730–8731.
68. Weinberg DR, et al. (2012) Proton-coupled electron transfer. *Chem Rev* 112(7): 4016–4093.
69. Lundberg M, Blomberg MRA, Siegbahn PEM (2004) Oxyl radical required for o-o bond formation in synthetic Mn-catalyst. *Inorg Chem* 43(1):264–274.